Magnetofriction – a new concept for shape memory composites

S. Hermann[1], **N. Muniz**[1], **M. Ouisse**[1], **L. Hirsinger**[2], **G. Chevallier**[1]

FEMTO-ST Institute, CNRS/UFC/ENSMM/UTBM, Besançon, France
[1] Applied Mechanics Department
[2] Micro Nano Sciences and Systems Department

E-mail: svenja.hermann@femto-st.fr, morvan.ouisse@femto-st.fr

October 18, 2022

Abstract. This paper introduces a new concept for shape memory based on elastic forces and magnetically induced friction forces in composite materials consisting of magnetoactive elastomers (MAEs). Magnetic attraction forces between two MAEs generate a contact pressure at their interface and the friction allows to maintain stable deformed shapes of the so-called Magnetofriction Shape Memory Polymers (MF-SMPs). When the contact is loosened, the friction forces vanish and the elastic forces in each part of the assembly bring the parts back into their initial state where the contact can be established once again. The shape memory effect is studied in three-point bending tests with two stacked MAEs. The global force-displacement relations reveal a hysteretic behavior due to local residual displacements after the test are observed by the help of digital image correlation (DIC). The test structure stores up to 25 % of the applied displacement. The local contact state (sliding or sticking) is evaluated in different regions of the MF-SMP which gives an insight into the shape memory mechanism magnetofriction. Two methods for the shape-recovery of the MF-SMP by elastic forces in the MAEs are proposed, a manual separation and an air flow at the interface of the MF-SMP, and a comparison of magnetofriction to other shape memory mechanisms is performed.

Keywords: Shape memory, magnetically hard magnetoactive elastomers (H-MAE), magnetic forces, frictional contact

Submitted to: *Smart Mater. Struct.*

1. Introduction

Materials or structures that exhibit a shape memory effect are capable to alter their shape between different stable states as a response to external stimuli. At least one stable state is memorized by the system [1] and the stable states allow for a shape control of the material. Possible applications for the shape memory effect can be found in the field of actuators, where different stable states are used to maintain positions without an external energy supply [2, 3]. Furthermore, a controlled repetitive shape change has been used in the field of soft robots to achieve different modes of locomotion [4] and to design biomedical applications [5].

The shape memory effect can be triggered by different physical stimuli in diverse types of materials. Two well-known activation mechanisms are a mechanical loading and a temperature variation which are applied to control shape memory alloys (SMAs) for example. SMAs are capable to recover seemingly permanent strains when heated due to a phase transformation between two stable phases: martensite and austenite [6]. The application of mechanical stresses to the low temperature martensite phase causes a reorientation from a twinned to a detwinned state. Heating the material results in a phase transformation into the austenite phase, whereby the strain is recovered. After cooling, the SMA recovers its twinned martensite state [7]. The shape memory effect in Shape Memory Polymers (SMPs) is based on the phase transition between the rubbery and the glassy state [8, 9]. After the cooling, a SMP memorizes the deformation that was applied in the high temperature state. The recovery of the initial shape is activated when the temperature increases above the glass transition temperature [10]. To activate the shape memory without heating the environment of SMPs, recent works propose to embed magnetic particles in the polymer and use inductive heating of Magnetic Shape Memory Polymers (M-SMPs) for the phase transition [11, 12]. SMAs are capable to develop high forces and SMPs can store high deformations. However, the thermal activation of phase transitions is generally slow and requires additional equipment to accelerate the temperature variation. In addition, a temperature hysteresis has to be considered in thermally activated shape memory materials.

The shape memory effect can also be activated by magnetic fields solely in Magnetic Shape Memory Alloys (M-SMAs). In the martensite phase, the magnetic domains of the magnetized M-SMA are coupled to the structural domains. Therefore, external magnetic fields can cause a reorientation of the martensite variants leading to a shape change [2]. The application of a mechanical loading or a differently oriented magnetic field brings the M-SMA back to its initial shape. The magnetic shape memory effect in M-SMAs is temperature dependent [13]. Permanently magnetized magnetically Hard MagnetoActive Elastomers (H-MAEs) show a shape memory effect in presence of external magnetic fields [14, 15]. An H-MAE consists of magnetically hard particles and an elastomer matrix [16]. It can be permanently magnetized and is mechanically soft at the same time (Young's Modulus between several kPa and several MPa [17, 18, 19]). Complex shape changes occur when the H-MAE presents regions

with different orientations of the magnetic moments that align with external magnetic fields. When the external field is switched off, the elastic forces bring the H-MAE back to its initial shape. The magnetic actuation that can be performed is very fast (for example M-SMA: <1 ms [2], H-MAE: 0.1 s [14]). However, the deformation capacity of M-SMA is comparatively low due to the stiffness of the material while H-MAEs need to be surrounded by a magnetic field constantly to stay in the deformed configuration.

This work presents a new concept for shape memory in which friction is used to maintain a stable state in an assembled composite. The use of friction forces to generate a self-locking state is known from piezoelectric (PE) motors [20]. In PE motors, oscillations of piezoelectric elements are transferred by frictional coupling [21]. Motions are generated by establishing and releasing contacts between the motor and the object in motion [22, 23]. PE motors generally have fast response times as the friction forces can be established and withdrawn instantly. However, establishing the contact pressure for the force transfer from the PE motor to the object in motion is challenging. High preloads could hamper the movement of the object and vibrations of the PE stator could be transferred [21].

The new concept for shape memory, presented in this study, aims to overcome some of the challenges in existing shape memory materials by using friction instead of a phase change to achieve shape memory. Magnetic attraction forces are used to generate the contact pressure at the interface of a shape memory structure that is composed of two H-MAEs. The use of magnetic forces in order to establish mechanical contacts has been explored in the context of vibration damping by friction [24, 25] with the goal to establish a moderate and well distributed contact pressure. In the present work, the stable state is maintained by adhesion in the contact interface. The corresponding concept of magnetofriction is presented in the next section, followed by the introduction of the test structure which is used in this study. The experimental tests, which have been performed to study the storage of a deformed shape on a global scale and the contact state on a local scale, are presented afterwards. Two suggestions for the recovery of the initial configurations are experimentally demonstrated in the subsequent section. Finally, the new concept is compared to the aforementioned common shape memory strategies in order to identify potential application fields for the shape memory effect achieved by magnetofriction.

2. New concept: shape memory by magnetofriction

The concept for shape memory in this work is based on the competing strength of elastic forces and magnetically induced friction forces. Friction forces occur in the contact interfaces of assembled composites, composed of at least two independent parts in contact. The forces depend on the contact pressure which maintains the assembly together. In a Magnetofriction - Shape Memory Polymer (MF-SMP), the contact pressure is established magnetically. An MF-SMP is assembled from permanently magnetized H-MAEs such that the magnetic attraction forces F_{mag} establish the pressure

in the contact interface and assure the integrity of the mechanical joint (Fig. 1 a, 1). The H-MAEs show a viscoelastic behavior and have a low mechanical stiffness. The assembled MF-SMP can hence easily be deformed by an externally applied displacement u_a up to a maximum value u_a^{max} for example. When the assembly is deformed, elastic shear stresses appear in the material (σ_{xy}) and at the interface (σ_t) due to friction (σ_f). According to Coulomb's friction law, friction forces maintain the adhesion between the contact interface up to a specific threshold that depends on the material pairing and the normal stress.

The evolution of the local contact state is depicted in Fig. 1 b. For a small mechanical loading, there is adhesion between the two parts and the assembly behaves like a single part. When the elastic constraints in the H-MAEs generate forces at the interface that exceed the sliding threshold, the parts start to move with respect to each other and (Fig. 1 b, state B). The contact state in the assembly is dependent on the local

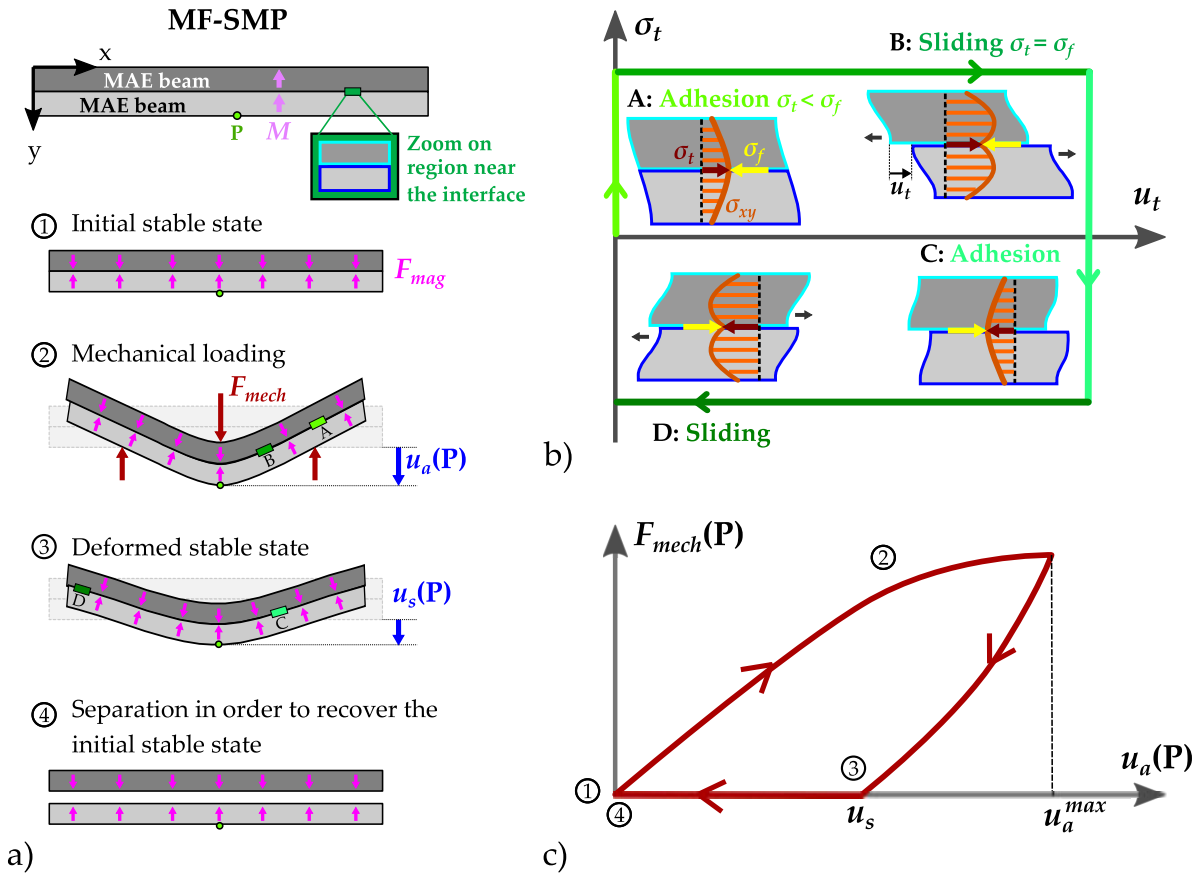

Figure 1. Schematic representation of the shape memory cycle of a Magnetofriction – Shape Memory Polymer assembled from two MAE beams: different states of the MF-SMP (a), local contact states the loading (b) and global relation between the reaction force and the displacement of the structure at point P (c). M : Magnetization, F_{mag} : magnetic forces, F_{mech} : mechanical reaction forces, u_a : applied displacement, u_s : stored displacement, σ_{xy} : shear stress, σ_t : tangential stress at the interface, σ_f : frictional stress, u_t : relative displacement, u_a^{max} : maximum applied displacement.

stresses, hence sliding and adhesion can both be present at the same time on different positions at the interface (Fig. 1 a, 2). The sliding releases a part of the elastic energy in the assembly. As the elastic constraints at the interface are decreased by the sliding, the contact state changes from sliding to adhesion at the end of the loading phase. The H-MAEs stick together once again due to the magnetically induced contact pressure.

When the mechanical loading is released, the elastic forces tend to bring each H-MAE back to its initial shape. They deform the MF-SMP and also generate restoring forces in the contact interface. At the interface, however, the restoring forces have to work against the friction forces. As a result, only a part of the applied deformation is restored as long as the friction forces are present (Fig. 1 a, 3). Locally, there is either sliding or sticking in the interface (Fig. 1 b, C and D). The MF-SMP is capable to store the deformation (illustrated by the stored displacement at point P $u_s(P)$ in Fig. 1 c) due to the friction at the interface.

When the magnetic attraction forces are reduced, the friction forces vanish and the elastic forces bring the parts of the assembly back into their initial shape. One possible solution to reduce the magnetic forces is the separation of the beams (Fig. 1 a, 4). The restoring of the contact pressure completes the shape memory cycle shown in Fig. 1 c. Since the shape memory effect is based on the magnetic forces and the resulting friction in the contact interface, it is called magnetofriction. The following section describes the study of an MF-SMP which is performed in order to proof the concept of shape memory by magnetofriction.

3. Materials and Methods

3.1. Design of the smart structure

The H-MAE used in this study is composed of magnetically hard NdFeB particles which are embedded in a silicone elastomer. The elastomer, also called matrix, is a viscoelastic material with a storage modulus in the order of magnitude of (1.5 ± 0.9) MPa in the rubbery state for a loading frequency of up to 100 Hz [18]. The particles have an average size of 5 µm and are dispersed randomly in the isotropic composite material. Since the particles are magnetically hard, the composite can be magnetized permanently. After the manufacturing, the composite is magnetized in a magnetic field of 4 T that magnetically saturates the particles. The H-MAE has a volume fraction of 36.2 % and a residual flux density of 0.3 T. The storage modulus lies in the order of magnitude between 2 MPa and 10 MPa depending on the temperature and frequency of the loading. More details about the elaboration and the behavior of this composite material can be found in [18].

Two H-MAE specimens are assembled to obtain the MF-SMP sample investigated in the present proof-of-concept study. They have a beam-like shape with the dimensions 60 mm × 6 mm × 3 mm (length × width × height). The beams are magnetized in the direction of their thickness and stacked such as their magnetization is oriented in the

same direction (Fig. 2). In this configuration, the specimens attract each other and a contact is established thanks to magnetic forces between the two MAEs in the MF-SMP.

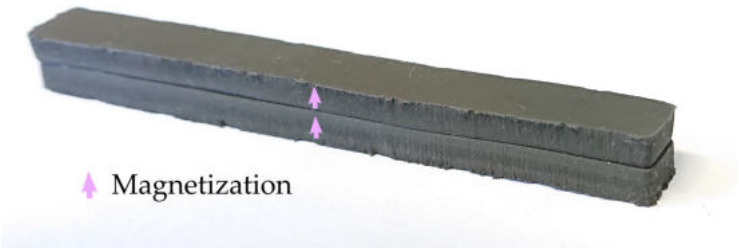

Figure 2. Magnetofriction Shape Memory Polymer (MF-SMP sample) assembled from two magnetized beams consisting of a magnetically hard magnetoactive elastomer (H-MAE).

3.2. Study of the deformation storage

3.2.1. Experimental setup and measurement protocol Three-point bending tests are performed with the MF-SMP and a single beam for comparison. The measurement setup, shown in Fig. 3a, is composed of two parts: a mechanical part, used to apply a loading and to measure the reaction forces, and an optic part used to record images for a digital image correlation (DIC) analysis. The specimens are positioned on the lower fixed part of the bending support in a dynamic mechanical analyzer (DMA). The distance between the two contact points of the lower support part measures 27.3 mm and the diameter of the cylinders which are in contact with the specimen measures 2.5 mm (see Fig. 3 b or c) The upper part of the DMA is deforming the specimen during the displacement-controlled bending test. It is positioned as close as possible to the specimen's surface without applying an initial loading prior to a test. During the test, the reaction force of a specimen is measured with a load cell connected to the lower support part. A lubricant is used to reduce the friction in the contact between the assembly and the bending test support. The test is filmed with a camera in order to perform the DIC later. The camera lens is positioned orthogonal to the specimen and films one side of the specimens. An additional lighting source is used to improve the image quality. The light reflected by the metallic particles in the beam is sufficient to obtain a good contrast in the image which is required for the DIC. Fig. 3b and Fig. 3c show the camera view of the assembled composite and the single beam respectively. The images are recorded with a frequency of 2 Hz and an analog voltage signal of the DMA machine was captured at the same frequency to associate an image to the force and displacement values.

The loading of the specimen is composed of different steps in order to observe the contact state for dynamic and static load cases. Fig. 4 illustrates the evolution of the applied displacement u_a, controlled and measured by the DMA machine on the mobile part. During the first of the four steps, the maximum displacement u_a^{max} is applied to the

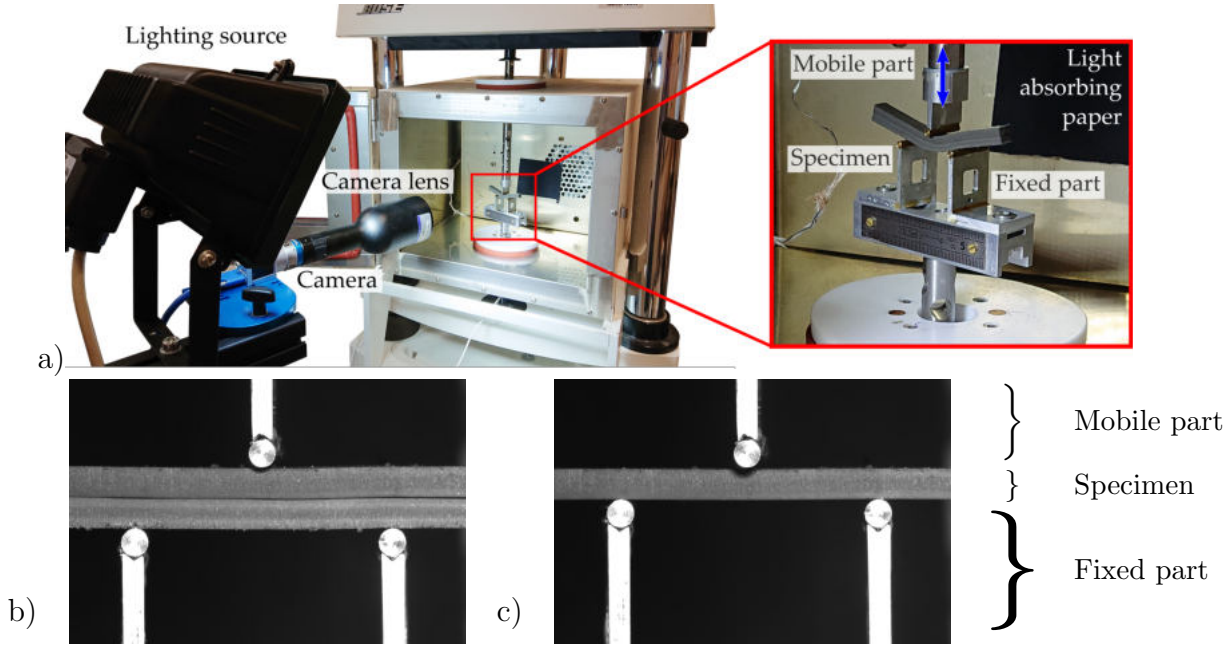

Figure 3. Experimental setup (a) and camera view on the assembled composite (b) and a single beam (c).

specimen. Afterwards, a cyclic loading with the amplitude u_{cyc} is applied and five cycles are performed around an average displacement of 2 mm. The specimen is not completely unloaded since the reaction force can only be measured when the experimental setup is composed of three unidirectional contacts (see Fig. 3 b or c). After the cyclic loading, the applied displacement u_a is kept constant at u_a^{max} for five minutes. In the last step, the loading is removed. The displacement velocity is kept constant at 0.12 mm/s during the loading and unloading steps. Five different amplitudes u_{cyc} have been tested : 1 mm, 1.5 mm, 2 mm, 2.5 mm and 3 mm.

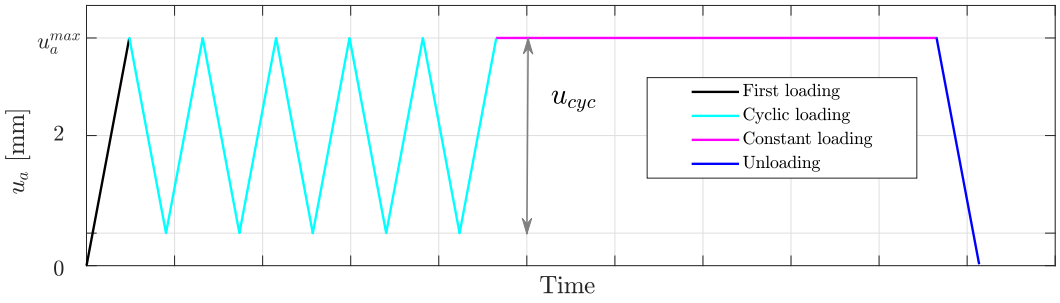

Figure 4. Target for the applied displacement u_a during the bending tests.

3.2.2. Post processing of the DMA data The applied displacement u_a and the reaction force F are obtained for the different steps of the bending tests. Force-displacement curves, such as represented in Fig. 5a, are used to compare the behavior of the two structures for different tested amplitudes. The results of the cyclic loading step allow

to calculate the apparent viscoelastic parameters of the two structures for each of the five cycles. The apparent stiffness k corresponds to the average slope of a load cycle (cf. Fig. 5b) and is obtained by a linear regression of all points of a single load cycle. For a given load cycle, the dissipated energy W_d corresponding to the area enclosed by the cycle is obtained by integration (Eq. (1)). The loss factor η allows to compare the two structures as it relates the dissipated energy W_d to the maximum elastic energy stored by the conservative part (W_s, Eq. (2)) during the load cycle. Practically, η is obtained by calculating W_d and k from the experimental results and using the relation shown in Eq. (3) where u_{cyc} is a controlled test parameter.

$$W_d = \oint_{1cycle} F \, \mathrm{d}u_a \tag{1}$$

$$W_s = \int_0^{u_{cyc}/2} k \, v \, \mathrm{d}v \tag{2}$$

$$\eta = \frac{W_d}{2\,\pi\,W_s} = \frac{4\,W_d}{\pi\,k\,u_{cyc}^2} \tag{3}$$

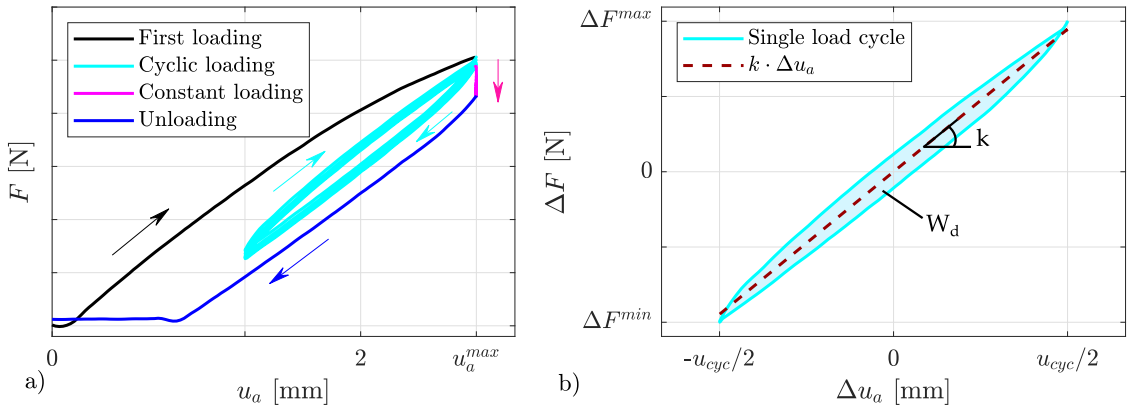

Figure 5. Example of a force-displacement curve obtained from a bending test (a) and variation of force and displacement of a single load cycle illustrating the stiffness k of a load cycle (b).

3.2.3. Post processing of camera images The camera images are evaluated with in-house algorithms. The first objective of the image evaluation is an analysis of the deformed shapes of the structures after the tests. Therefore, a surface line corresponding to the lower boundary of the single beam and the contact interface of the MF-SMP have to be detected in the images of the test. The evaluation is based on luminosity gradients in the images. Fig. 6a and d show the color gradient in an image of the single beam and the MF-SMP respectively. The red line represents a position for which the surface line has to be detected and the corresponding luminosity values for the pixels are represented

in Fig. 6b and e. For the single beam, the lower surface has to be detected while the interface is searched for the MF-SMP. The black dots in Fig. 6b and e mark the points for the position of the red line. By detecting the points on every horizontal position in the images, the corresponding surface lines are identified as Fig. 6c and f exemplary show for one image. The procedure is repeated for every image of the test.

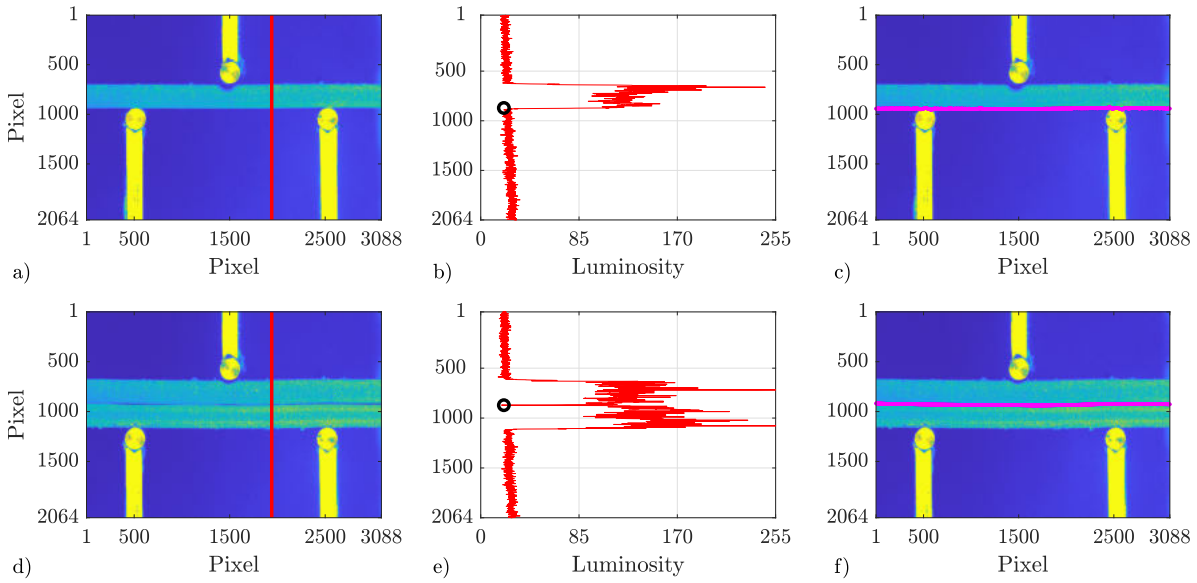

Figure 6. Illustration of the surface detection procedure in images of the single beam (upper line) and the MF-SMP (lower line): luminosity gradient of the camera images with horizontal position 1940 marked in red (a, d), corresponding luminosity values (b, e) and detected interfaces in the images (c, f).

The second objective of the image evaluation is the analysis of the local contact state (sticking or sliding) in the MF-SMP. On this purpose, the relative movement of spatially close regions in the upper and lower beam are traced during the bending test. The tracing is based on a cross correlation between luminosity patterns of two different regions. A region is defined as a 5×5 pixel area around a central pixel, as illustrated by the blue dot and the red square in Fig. 7 a. To trace the pixel region during the test, a search region of 11×11 pixels is defined around the central pixel and (black square in Fig. 7a). From the second to the last camera image, the traced region (red square) is identified in the search region (black square) by the help of a cross correlation. The position of the central pixel and the regions are updated for the research in the following image. Fig. 7b exemplary shows a pixel pair in region of the MF-SMP highlighted by a white square in Fig. 7c. The analysis of their relative movement allows to determine the contact state of the surrounding area. On this purpose, their positions are traced throughout the test. Afterwards, their positions are evaluated with respect to the interface such that the distance towards the interface ("normal distance") and their relative distance in the direction of the interface ("tangential distance") are calculated.

Normal and tangential directions vary with the position on the interface, as Fig. 7c shows, but since the pixel regions are chosen close to each other the tangential distance can be approximated by a straight line.

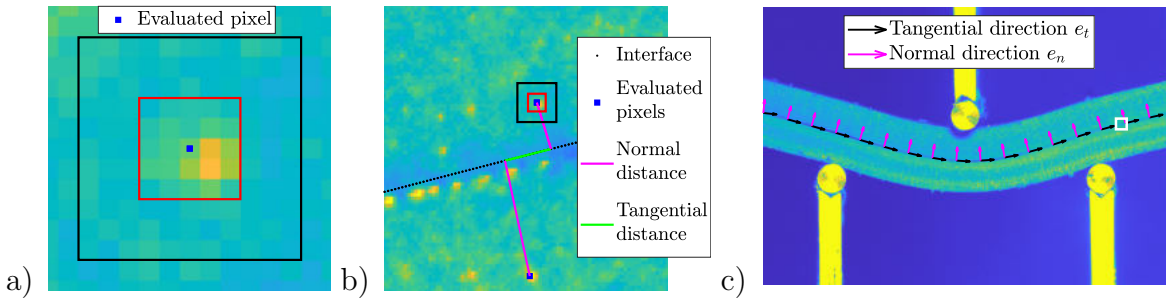

Figure 7. Illustration of the contact state analysis: Pixel region (red square) around a central pixel to be traced in a search region (black square) (a), two pixels evaluated for the contact state detection and corresponding parameters (b) and illustration of the normal and tangential directions linked to the interface (c).

The local contact state is evaluated in 13 regions on the MF-SMP for each of the three tests. On this purpose, 13 pixel pairs (PPs) are chosen along the beam with one pixel of each pair belonging to the upper beam and the other to the lower beam. Fig. 8 illustrates the choice made for the test with $u_{cyc} = 2.5\,\text{mm}$, the choice for the other two amplitudes can be found in Appendix A. The tangential displacement u_t between the pixel pairs is calculated in the direction e_t (defined in Fig. 7 c) as the variation of the tangential distance. A value of u_t different from zero corresponds to sliding, more specifically: an increase of u_t means that the upper beam moves in the tangential direction with respect to the lower beam and a decrease of u_t represents the opposite movement. The size of the pixels in the images is 0.12×0.12 mm, this relation is used to convert the positions and distances.

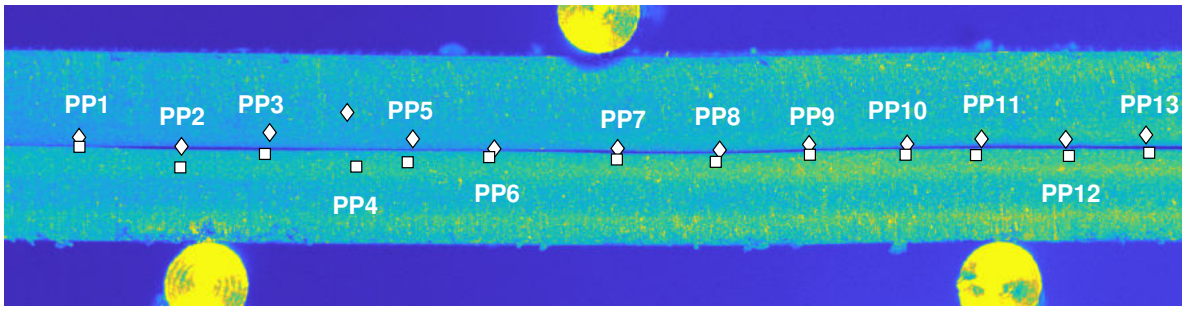

Figure 8. Choice of the pixel pairs (PPs) along the MF-SMP for the evaluation of for the test with $u_{cyc} = 2.5\,\text{mm}$. $\diamond$ – pixel in upper beam, $\square$ – pixel in lower beam

3.3. Initial shape recovery

To recover the initial shape, the friction forces in the contact interface of the MF-SMP have to be overcome. Without the friction, the elastic forces restore the initial shape of

the two beams. A convenient solution for this is to suppress the normal forces by simply separating the beams. Two methods for the separation of the beams are tested with a cantilevered MF-SMP. The structure is deformed manually at the beginning of the tests. In the first test, they are separated manually afterwards (Fig. 9a). In a second test, an air-flow at the interface is used to separate the beams temporarily. On this purpose, a tube is inserted in the clamping of the assembled composite as Fig. 9b shows. Due to the magnetic attraction forces, the beams should stick together once again after their separation in both cases.

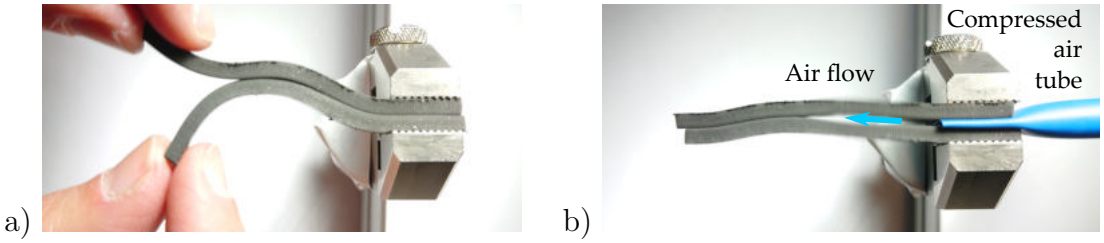

Figure 9. Recovery of the initial shape by separation of the magnetized beams in the MF-SMP: manual separation of the beams (a) and separation of the beams by an air flow at the interface (b).

4. Results and Discussion

This section presents the analysis of the shape memory in the MF-SMP. In a first time, the stable deformed shapes of the single beam and the MF-SMP after the test are compared qualitatively. A more detailed qualitative analysis of three results obtained with the MF-SMP is performed subsequently to better understand the shape memory mechanism. Therefore, the stored displacement of both structures after the tests is evaluated by the help of the camera images. The reaction force of the two structures to the deformation is compared and their viscoelastic behavior is evaluated. Finally, the local contact state in the MF-SMP is evaluated at different positions near the interface.

4.1. Displacement storage

The stored displacements of the structures after the tests are evaluated by the help of the camera images. The positions of the lower surface of the single beam and the interface of the MF-SMP are determined at the beginning and the end of the test. The stored displacements u_s of the points constituting the interfaces are calculated from the DIC analysis as the position difference before and after the test. The results are normalized with respect to the highest displacement amplitude, corresponding to 0.424 mm. The normalized interface displacements u_{sn} of the single beam and the MF-SMP are shown in Fig. 10 a and b respectively. In general, both structures remain deformed after the test with the exception of two tests with the single beam at the lowest amplitude. We conclude that the displacement storage of the single beam can be caused by its

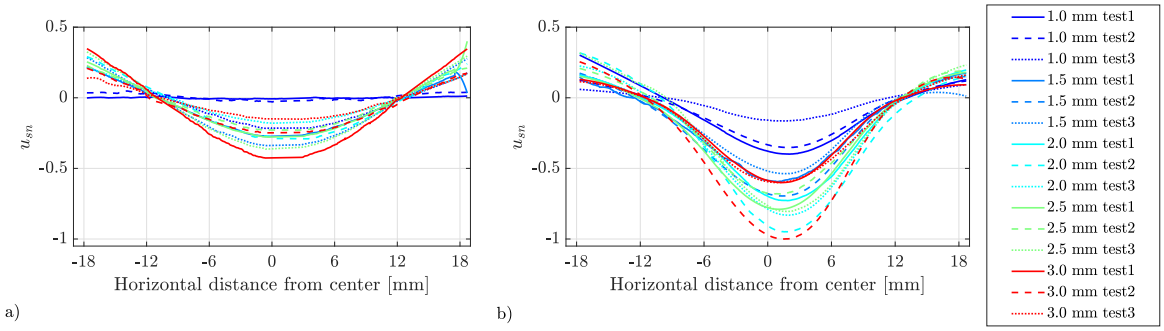

Figure 10. Normalized stored displacements, u_{sn}, obtained for the single beam (a) and the MF-SMP (b) after the bending tests.

viscoelastic behavior or friction between the structure and the experimental setup. These effects are hence also present for the MF-SMP. Nevertheless, the permanent deformation is higher for the MF-SMP than for the single beam in most cases. The deformed shapes of the two structures show an interesting difference: while the shape of the single beam has a symmetric parabolic shape, the outer ends of the displacement curves of the MF-SMP are inclined and the shape of the curves is less symmetric. The behavior of the MF-SMP is caused by the relative displacement field at the interface which is not symmetric with respect to the center of the specimen. The non-symmetric sliding field is shown in this section (Paragraph 4.3 (Fig. 16).

The maximum displacement amplitudes stored in the central region of the two structures, $u_{sn}^{max}|\min(u_{sn})|$, are represented for the tests with different controlled amplitudes u_{cyc} in Fig. 11 a and b respectively. The graphic highlights the scatter of the measurement results for single amplitudes which is already observable in Fig. 10. The specimen has to be removed from the machine after each test and the MF-SMP is reassembled which leads to the scattering as the interface conditions change. However, the measurement results show clear trends as the average values and standard deviations

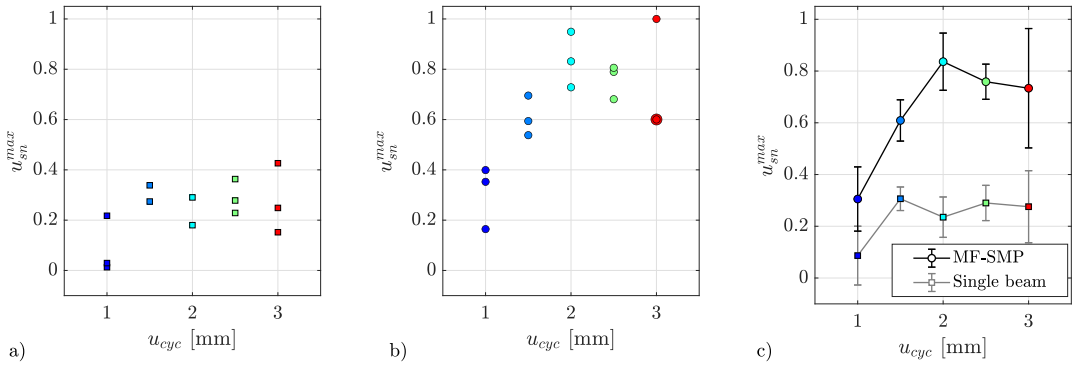

Figure 11. Maximum normalized stored displacement amplitudes, u_{sn}, obtained for the single beam (a) and the MF-SMP (b) and average values and standard deviations for both structures (c).

in Fig. 11 c illustrate. The stored displacement of the two structures is similar for the smallest applied displacement. We conclude that the loading of the MF-SMP has to be sufficiently high to overcome the friction threshold in the contact interface in order to trigger the shape memory. For higher amplitudes of u_{cyc} the displacement storage is higher for the MF-SMP which corresponds to a stronger shape memory. The maximum displacement of the MF-SMP increases strongly up to an amplitude of $u_{cyc} = 2\,\text{mm}$. The evolution for higher values of u_{cyc} is less clear but the increase is strongly reduced.

In order to analyze the mechanisms of magnetofriction in detail, three tests with the respective cyclic amplitudes of 1.5 mm, 2.5 mm and 3 mm have been evaluated. The stored displacements u_s obtained for these tests are shown in Fig. 12. For the MF-SMP, the displacement storage is maximized for $u_{cyc} = 2.5\,\text{mm}$. The lowest displacement storage is obtained for the highest applied amplitude of $u_{cyc} = 3.0\,\text{mm}$, which is counterintuitive at first. For this amplitude, the stored displacement is even close to the displacement stored by the single beam and could hence be caused by viscoelastic effects or friction between the structure and the experimental setup.

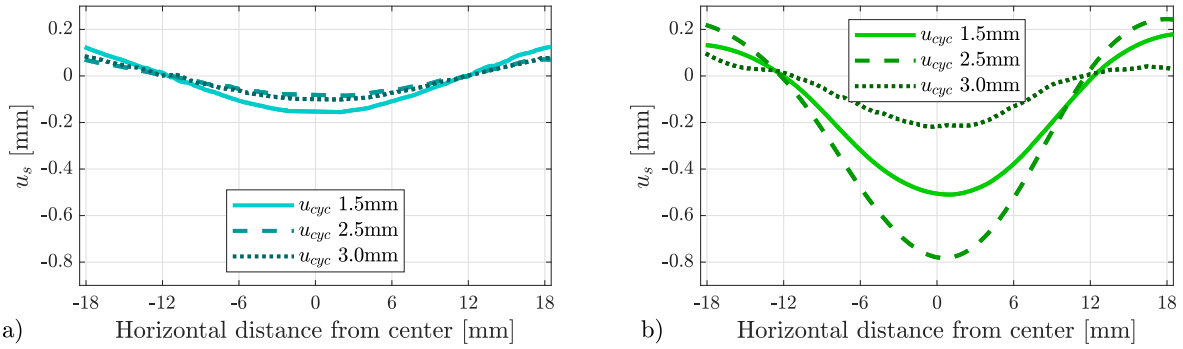

Figure 12. Stored displacements u_s obtained for the single beam (a) and the MF-SMP (b) at three different amplitudes u_{cyc}.

To evaluate the displacement storage capacity of the structures, the ratio between the maximum applied displacement and stored displacement, U, is calculated. As the structures are not in contact with the machine at the beginning of the test, the real displacement of the specimen, u_r, is slightly smaller than the applied displacement u_a. To determine the real maximum displacement u_r^{max}, the position variation of the interfaces are evaluated with respect to the initial position in the first camera image. The maximum amplitudes of the applied displacement (u_a^{max}) and the real displacement (u_r^{max}) as well as the maximum value of the stored displacement ($u_s^{max} = |\min(u_s)|$) are summarized in Tab. 1. The results show, that the MF-SMP is capable of storing up to 25.5 % of the applied deformation in the configuration presented in this study. To better understand the mechanisms that lead to the amount of displacement storage, a study of the contact state in the MF-SMP has been performed and is presented in the next section.

Table 1. Results obtained for the maximum applied displacement u_a^{max}, the real maximum displacement u_r^{max}, the maximum stored displacement u_s^{max} and their ratio U

u_{cyc} [mm]	Specimen	u_a^{max} [mm]	u_r^{max} [mm]	u_s^{max} [mm]	$U = u_s^{max}/u_r^{max}$ [%]
1.5	Single beam	2.75	2.56	0.20	7.8
	MF-SMP		2.57	0.51	19.8
2.5	Single beam	3.25	3.06	0.10	3.3
	MF-SMP		3.06	0.78	25.5
3.0	Single beam	3.50	3.35	0.12	3.6
	MF-SMP		3.22	0.22	6.8

4.2. Global force displacement relations

Fig. 13 a exemplary shows the evolution of the reaction force of the MF-SMP obtained from a test with $u_{cyc} = 1.5\,\text{mm}$. Tendencies like the decreasing average force during the cyclic loading and a force decrease during the constant loading, due to viscoelastic stress relaxation, are observed in all tests. The evolution of the force-displacement curve in Fig. 13 b reveals some characteristics of the first loading and final unloading phase which are caused by the test setup and the measurement protocol. Firstly, the reaction force does not increase instantly with the applied displacement because the contact is not established at the beginning of the test. Prior to the test, the upper support part is manually brought as close as possible to the specimen without touching it which causes the small delay at the beginning of the test. Secondly, the force passes by a minimum during the unloading phase and stabilizes at a constant offset value different from zero. The existence of the minimum point can be explained by the loosening of the contact between the upper support part and the specimen. The camera images show that the structure sticks to the upper support part for a short time during the unloading. In this

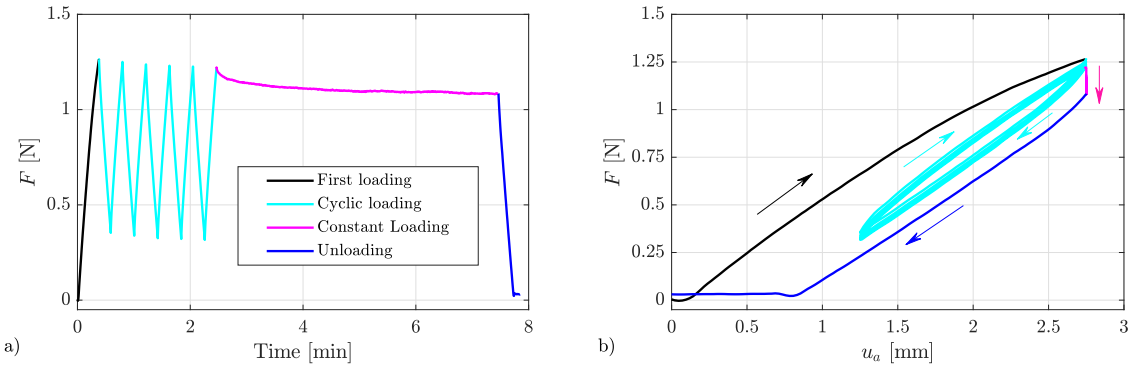

Figure 13. Reaction force of the MF-SMP to a loading with a cyclic displacement amplitude of $u_{cyc} = 1.5\,\text{mm}$ as a function of the time (a) and the displacement amplitude u_a (b).

configuration, the support part pulls on the specimen until the weak adhesion forces are overcome by the gravitational forces and the contact is loosened. The force offset at the end of the test is due to the configuration of the load cell. As all test results show these characteristics, they are considered as inherent to the test method.

The force-displacement curves of all tests are shown in Fig. 14. The absolute values of the reaction forces are higher for the MF-SMP as the structure has twice the thickness of the single beam. The shape of the load cycles (cyan) is more symmetric for the MF-SMP as for the single beam. The pointed ends of the cyclic loading of the MF-SMP are an indicator for a system with friction, since a viscoelastic behavior would generate ellipsis with rounder ends. The five load cycles of each test are used to calculate the apparent viscoelastic parameters of the structures for each load amplitude. The average values and corresponding standard derivations are summarized in Tab. 2.

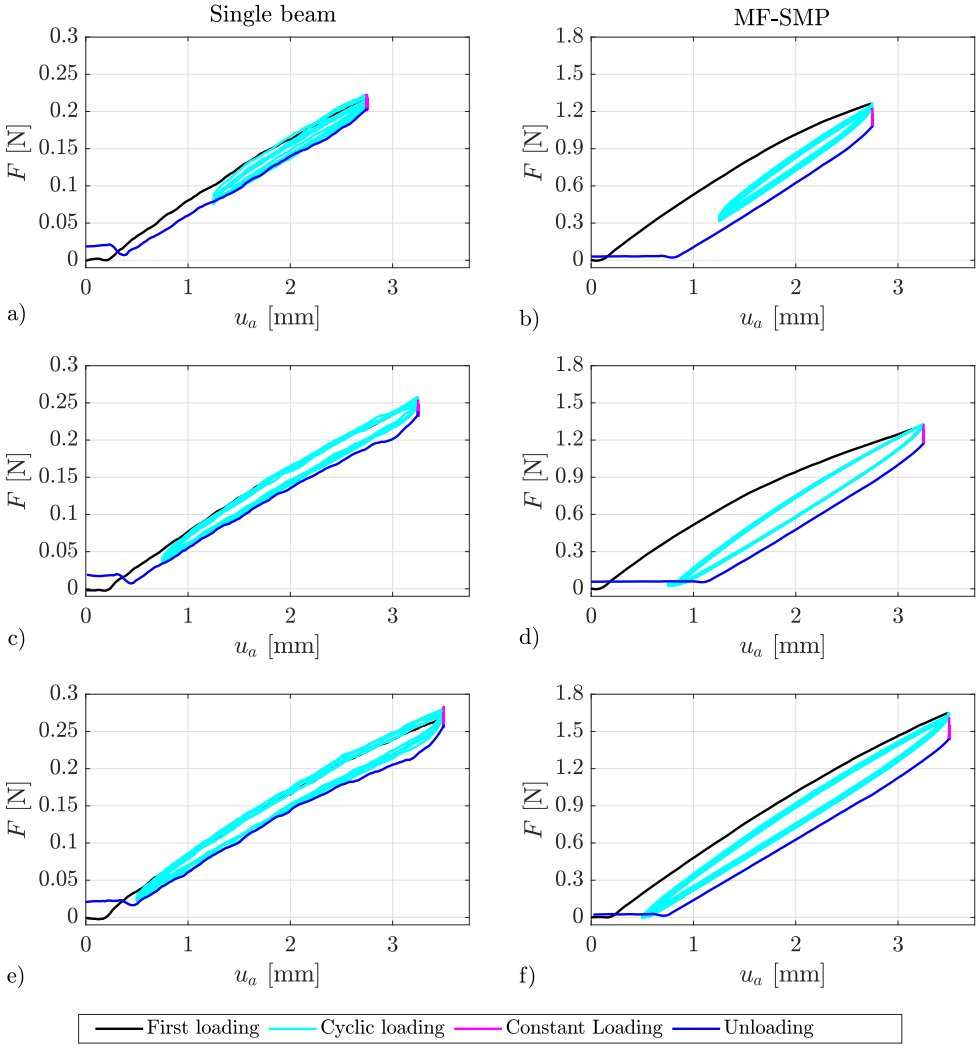

Figure 14. Force-displacement curves obtained for the single beam (left column) and the MF-SMP (right column) for displacement amplitudes of $u_{cyc} = 1.5\,\text{mm}$ (a, b), $u_{cyc} = 2.5\,\text{mm}$ (c, d) and $u_{cyc} = 3.0\,\text{mm}$ (e, f).

Table 2. Viscoelastic parameters (stiffness k, dissipated energy W_d and loss factor η) of the single beam and the MF-SMP obtained from the test with different amplitudes u_{cyc}

u_{cyc} [mm]	Specimen	k [N/m]	W_d [μJ]	η [%]
1.5	Single beam	86 ± 1	19 ± 4	13.0 ± 2.5
	MF-SMP	582 ± 3	108 ± 1	10.7 ± 0.1
2.5	Single beam	82 ± 1	41 ± 5	10.4 ± 1.4
	MF-SMP	523 ± 3	291 ± 15	11.4 ± 0.6
3.0	Single beam	79 ± 1	60 ± 4	10.7 ± 0.8
	MF-SMP	532 ± 1	361 ± 2	9.6 ± 0.1

The stiffness k and dissipated energy W_d of the MF-SMP are higher than the stiffness of the single beam due to the geometry difference mentioned before. The structures can be compared by the help of the loss factor η, as it includes the ratio of stored and dissipated energy (cf. Eq. (3)). The results obtained for the two structures and three amplitudes are very similar The presence of friction would have a significant influence on the loss factor when the load amplitude changes. In conclusion, dissipation by friction does not play a significant role during the cyclic loading under the conditions chosen in this study.

However, several characteristics of the force-displacement curves indicate the presence of a phenomenon in the MF-SMP that is not present in the single beam. A major difference between the two structures is the evolution of the reaction force during the first two steps of the test. For the single beam, the reaction force to the first loading is similar to the loading path of the cyclic test. For this reason, the first loading path is barely visible for the single beam in Fig. 14a, c and e. For the MF-SMP, there is always difference between the first loading path and the reaction forces during the cyclic loading (Fig. 14b, d and f). This behavior can be explained by magnetofriction. During the first loading, the friction forces at the interface of the MF-SMP are overcome and the beams start to slide over each other. A part of the deformation is stored by friction and the cyclic loading is hence performed on the pre-deformed MF-SMP. In this deformed configuration, the elastic restoring force is smaller than in the non-deformed configuration and the MF-SMP opposes less to the deformation.

An additional difference between the MF-SMP and the single beam is the evolution of the average force during the cyclic loading (centers of the loading cycles in Fig. 14). For both specimens, the average forces for $u_{cyc} = 3\,\text{mm}$ is approximately 3 % higher than for $u_{cyc} = 1.5\,\text{mm}$. But while the average forces of the single beam are similar for $u_{cyc} = 2.5\,\text{mm}$ and $u_{cyc} = 3\,\text{mm}$, the average force of the MF-SMP drops of almost 30 % from $u_{cyc} = 1.5\,\text{mm}$ to $u_{cyc} = 2.5\,\text{mm}$. Considering the fact that the difference between the first loading and the cyclic loading is the biggest for $u_{cyc} = 2.5\,\text{mm}$ the assumption that more of the deformation is stored for this amplitude than for the two others can

be put forward. The deformed shape of the two structures is analyzed in the following section.

4.3. Local contact state

The tangential displacements u_t are evaluated in the following to reveal the contact state (sticking or sliding) in the MF-SMP. Fig. 15 b illustrates the results obtained for pixel pair PP10 (cf. Appendix Fig. A1) obtained from the test with $u_{cyc} = 1.5\,\text{mm}$. The comparison with the applied displacement u_a in Fig. 15 a shows that the different steps of the test can be identified in the tangential displacement of the pixels. The early increase of u_t shows that the beams start to slide over each other almost from the start of the test in the region of pixel pair 10. There is a small variation of the tangential displacement during the cyclic loading, but value of u_t is similar before and after the cyclic loading. This result shows that a cyclic loading does not contribute in a significant manner to the deformation storage. Neither does the constant loading for which u_t increases only weakly.

During the unloading phase, u_t decreases which means that the direction of relative displacement in the region of PP10 is inverted. The beams slide over each other in the opposite direction but do not reach the initial configuration as u_t does not return to zero at the end of the test. This difference represents a displacement storage. The camera has been stopped approximately one minute after the end of the test to analyze an eventual influence of the viscoelastic shape recovery on the tangential displacement. Since the value remains almost constant after the unloading, this influence not significant in the

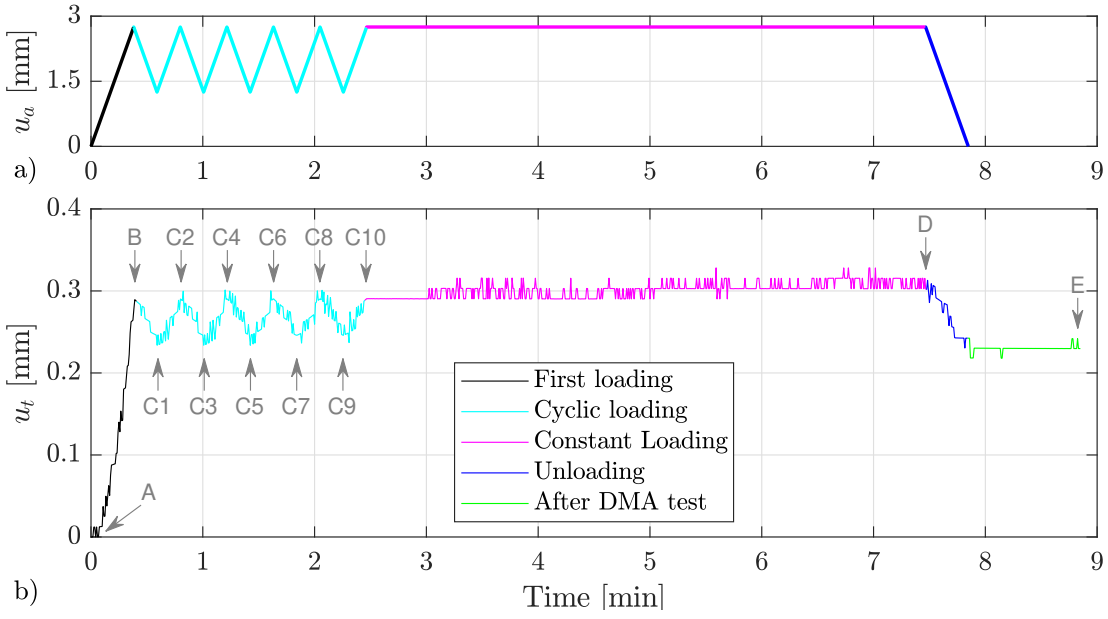

Figure 15. Applied displacement u_a (a) and tangential displacement u_t (b) on PP10 in a test with $u_{cyc} = 1.5\,\text{mm}$.

Table 3. Summary of the different instants of the tests (A to E, cf. Fig. 15) which are used to calculate the variation of the tangential displacement Δu_t.

Step	Instants used for the calculation of Δu_t
First loading	B-A
Cyclic loading	C2-C1, C4-C3, C6-C5, C8-C7, C10-C9
Cyclic unloading	C1-B, C3-C2, C5-C4, C7-C6, C9-C8
Constant loading	D-C10
Unloading	E-D

present tests. This result can be due to the small velocities in the present tests, the effect should be analyzed in tests with higher applied displacements and velocities where a higher amount of viscoelastic recovery is to be expected. The constant value of u_t shows that the sliding stops with the end of the test for PP10.

The relative displacement u_t in the different loading and unloading phases is compared for the three tests with the MF-SMP in the following. Therefore, the variation of u_t, Δu_t, is calculated between 13 different instants of the test. Fig. 15 shows the instants A to E, Δu_t is calculated between all subsequent instances and associated to the steps shown in Tab.3. The variation of the tangential displacement in the different steps is calculated for all pixel pairs and for the three tests with different amplitudes. The results are represented in Fig. 16 where the values obtained from the example above are highlighted with filled dots.

In Fig. 16, the values of Δu_t are separated in steps that represent a loading of the MF-SMP (left column) and steps that represent an unloading of the MF-SMP (right column). The position of the contact points with the upper and lower support part are represented by grey rectangles in the graphics. In general, the displacement variation is symmetric due to the symmetric test configuration. During the unloading phases, Δu_t is opposed to the loading phases which corresponds to the observation in the example above. The strongest variations of u_t are obtained in the regions between the contact points with the machine since the regions near the contact zone experience an additional contact pressure from the support parts. By comparing the results of the three different amplitudes, the contact mechanics during the tests becomes more comprehensible. The highest relative displacements are obtained for $u_{cyc} = 2.5\,\text{mm}$. This test shows the highest values for Δu_t during the first loading. The displacement variation during the final unloading phase is similar to the variation observed for $u_{cyc} = 1.5\,\text{mm}$, but since the variation during the first loading is smaller the MF-SMP remains less deformed at the end of the test. The results for $u_{cyc} = 3.0\,\text{mm}$ show two main differences compared to the other tests. Firstly, the magnitude of Δu_t during the unloading is very similar to the displacement during the first loading. In this case, the relative displacement is almost not stored by friction and, as a results, the MF-SMP remains almost non-deformed after the test. Secondly, the magnitude of Δu_t during the cyclic loading corresponds to the magnitude of the first loading. This behavior could be caused by the

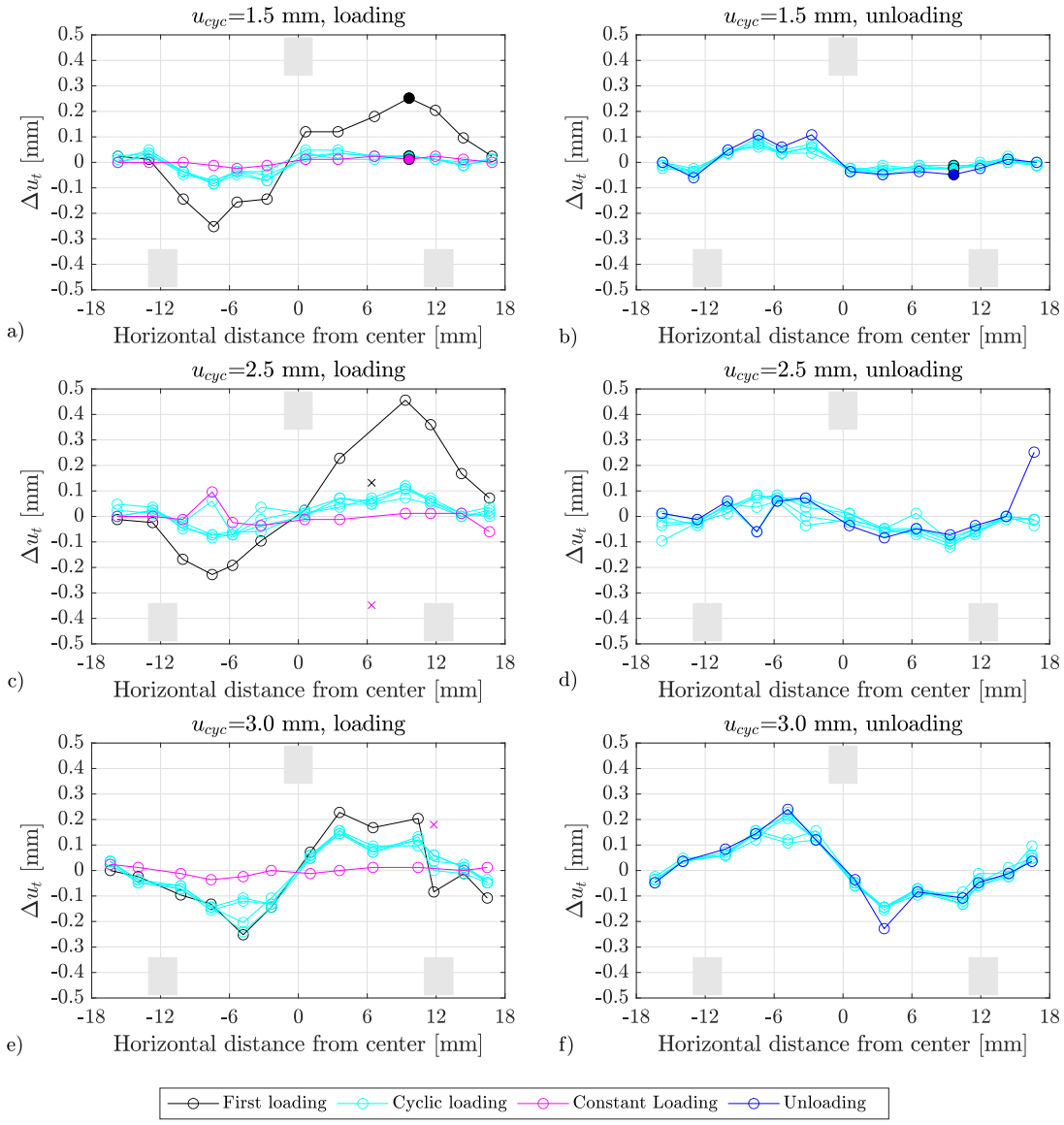

Figure 16. Variation of the tangential displacements Δu_t during the different steps of the tests with different u_{cyc}, causing either a loading (left column) or an unloading (right column) of the MF-SMP. × – displacement not correctly identified, ■ – Positions of support parts in the setup.

elastic restoring forces being strong enough to overcome the friction forces and provoking sliding. In summary, the analysis of Δu_t give an insight in the contact mechanics of the magnetofriction present in the MF-SMP. While this proof-of-concept study aims to understand the basic mechanisms that lead to the displacement storage, an important step for future studies is the understanding of different parameters that influence the amount of displacement that can be stored like the composition of the H-MAE beams, their surface characteristics or the assembly of the MF-SMP.

4.4. Initial shape recovery

The two methods proposed for the recovery of the initial shape have been tested successfully as Fig. 17 shows. In both cases, the shape memory effect was activated manually and stayed in a deformed stable state. After the manual separation, the beams were brought close to each other to reassemble due to the magnetic forces and a shape similar to the initial shape could be achieved. The separation by air flow also works well and the MF-SMP reassembles automatically when the air flow is stopped. However, the flexibility of the beams is a challenge for the recovery of the exact initial shape. Due to the magnetic forces, the beams attract each other when their distance is small enough. In tests with a strong air flow, the single beams deform a lot and sometimes reassemble in a configuration different from the initial shape. Hence, the optimum shape recovery strategy for the MF-SMP should separate the single beams

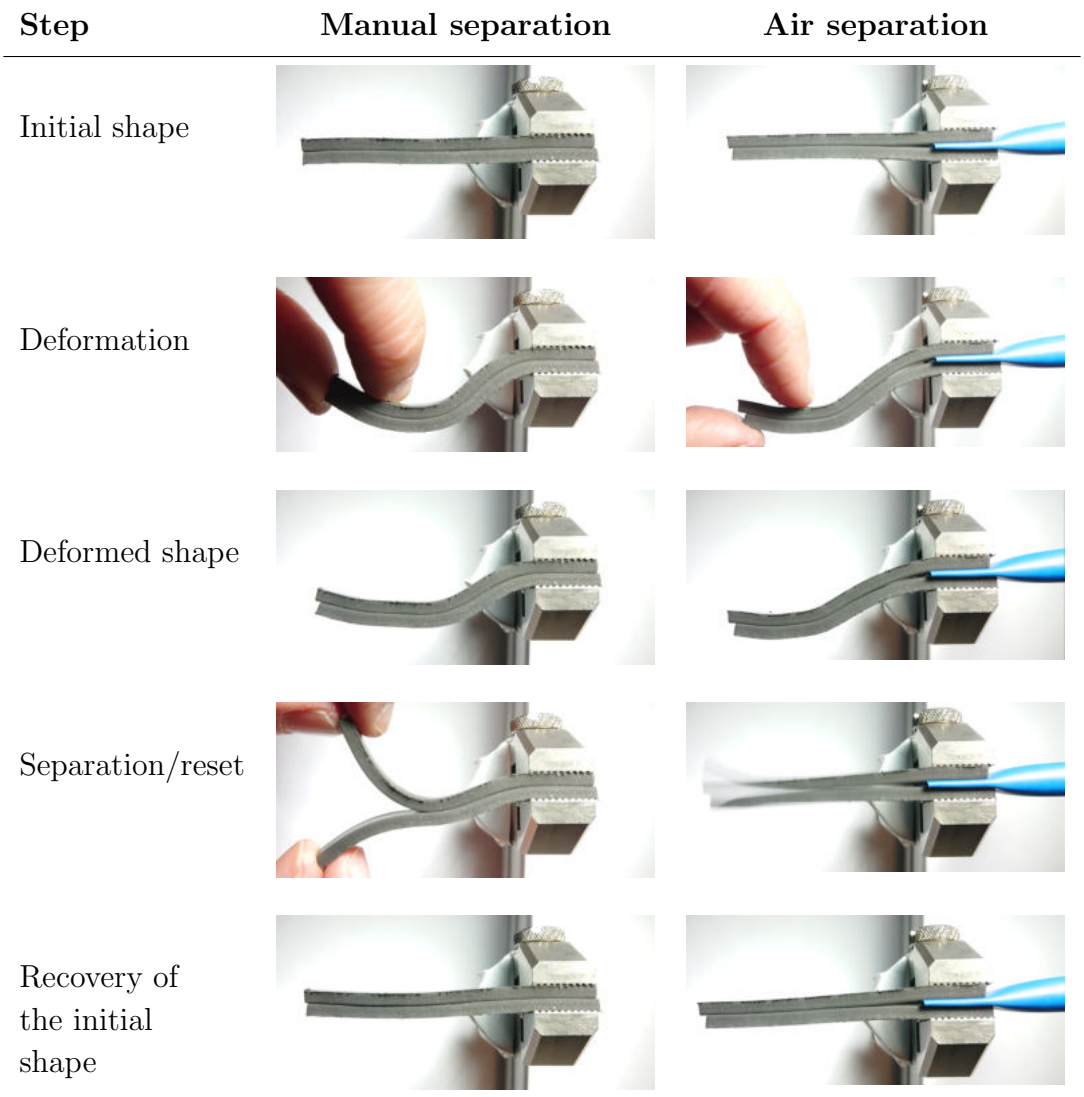

Figure 17. Proposed methods for the initial shape recovery of a cantilevered MF-SMP: manual separation and air flow at the interface.

but prevent the MF-SMP from reassembling in another deformed configuration. The restoring of the initial shape will hence be one of the challenges for future works.

5. MF-SMP compared to other shape memory materials

Magnetofriction is a new concept for shape memory proposed in this proof of concept study and the performance of the structure is not optimized. Therefore, a qualitative comparison with other shape memory materials aiming to position the new concept in the field of existing shape memory strategies is presented in this section.

Magnetofriction offers an advantage concerning the activation time of the shape memory effect as the effect is activated instantly when the adhesion threshold is exceeded in the contact interface. The recovery of the initial shape has been achieved instantly as well in the compressed air tests. The time constant of the MF-SMP is, thus, more similar to the magnetically activated M-SMA and H-MAE than to thermally activated SMA or SMP. The MF-SMP is well suited for shape memory mechanisms which require fast actuation cycles.

The mechanical stiffness of the MF-SMP in its stable states lies below the stiffness of almost all shape memory materials, besides the H-MAE. Possible application cases can, therefore, be found in research fields that are promising for H-MAE like in biomedical applications or in soft robotics where the mechanical compliance is required. In contrast to an H-MAE, the MF-SMP locks a deformed shape without the need of an external stimulus. H-MAEs remain deformed in a deformed shape only in presence of external magnetic fields. Therefore, MF-SMPs are favorable for applications in which stable states need to be maintained over a long time.

The comparison of the different materials offers perspectives for future work on MF-SMP with the objective to achieve higher performances in terms of the shape memory. In this study, the MF-SMP was capable to memorize up to 25 % of the applied deformation

Table 4. Properties of different shape memory alloys in qualitative comparison: Shape Memory Alloys (SMA), Shape Memory Polymers (SMP), Magnetic Shape Memory Alloys (M-SMA), magnetically Hard Magnetoactive Elastomers (H-MAE) and the Magnetofriction Shape Memory Polymer (MF-SMP).

Criteria	SMA [26, 7]	SMP[27, 10]	M-SMA[28, 2]	M-SME [14]	MF-SMP
Material	NiTi	Veriflex®	Ni-Mn-Ga	Silicone+NdFeB	Silicone+NdFeB
Activation type	Mechanics, Temperature	Mechanics, Temperature	Mechanics, Magnetism	Mechanics, Magnetism	Mechanics, Magnetism
Activation time	●●○	●○○	●●●	●●●	●●●
Stiffness (T_{amb})	●●●	●●○	●●●	●○○	●○○ [18]
Shape change capacity	●●●	●●●	●○○	●●○	●●○
Self-sufficient deformed state	✓	✓	✓	×	✓

and to recover the initial shape after reset by separation. Compared to the high shape change capacity of SMA and SMP, this performance is not outstanding, but is has to be reminded that the MF-SMP in this study was not optimized at all. Additional studies should be performed with the objective to optimize the shape memory in MF-SMP which will allow a quantitative comparison of the amount of stored deformation, the activation time or the stiffness variation during the transition for example.

6. Summary and Conclusions

In this study, the concept of magnetofriction is proved as a new method for shape memory in assembled composites based on magnetized magnetoactive elastomers (H-MAEs). The concept, presented in the first part of the paper, uses friction between magnetized MAEs to maintain a stable deformed state of the assembly, called Magnetofriction Shape Memory Polymer (MF-SMP). The initial shape can be recovered by the elastic forces in the beams when the latter are separated. The concept is proved and studied experimentally in the present work. Three-point bending tests are performed with a MF-SMP composed of two stacked H-MAE beams and a single beam for comparison. The analysis of the shape memory mechanism involve the evaluation of viscoelastic parameters and the use of digital image correlation algorithms to detect interfaces and moving regions in the MF-SMP. Analysis of the force-displacement curves and the local contact state reveal that the beams of the MF-SMP are principally sliding over each other during the first loading and that the friction stores this relative displacement. The residual deformation of the MF-SMP after the test is dependent on the applied deformation of the structure and displacements up to 25.5 % can be stored by the structure. The recovery of the initial shape has been performed by manual separation end the introduction of an air flow at the interface. A qualitative comparison of magnetofriction to other shape memory mechanism shows that the MF-SMP is suitable for applications that require fast actuation, a passive shape memory and mechanical compliance at the same time.

The present work is a proof of concept study. Now that the shape memory mechanism of magnetofriction is understood, an important next step is to find out how the different friction parameters influence the shape memory effect. The influence of the contact pressure could be studied with MAEs presenting different volume fractions of NdFeB particles as the intensity of the magnetic forces is linked to the particle content in the composite. Using MAEs with differently structured surfaces in MF-SMP assemblies will give an insight in how the surface characteristics influence the shape memory effect. The identification of these parameter will allow the design of optimized MF-SMP with a high capacity to store deformations and to recover the initial shape. Eventually, the capacity to design efficient shape memory material will pave the way for new devices based on magnetofriction.

Acknowledgments

This work has been funded by the EIPHI Graduate School, ANR-17-EURE-0002.

References

[1] M. Bengisu and M. Ferrara. *Materials that move: smart materials, intelligent design*. Springer, 2018.

[2] M. Kohl, M. Gueltig, V. Pinneker, R. Yin, F. Wendler, and B. Krevet. Magnetic shape memory microactuators. *Micromachines*, 5(4):1135–1160, 2014.

[3] P. Motzki, F. Khelfa, L. Zimmer, M. Schmidt, and S. Seelecke. Design and validation of a reconfigurable robotic end-effector based on shape memory alloys. *IEEE/ASME Transactions on Mechatronics*, 24(1):293–303, 2019.

[4] W. Hu, G. Z. Lum, M. Mastrangeli, and M. Sitti. Small-scale soft-bodied robot with multimodal locomotion. *Nature*, 554:81–85, 2018.

[5] P.R. Buckley, T.S. McKinley, G.H. andWilson, W. Small, W.J. Bennett, J.P. Bearinger, M.W. McElfresh, and D.J. Maitland. Inductively heated shape memory polymer for the magnetic actuation of medical devices. *IEEE Trans. Biomed. Eng.*, 53:2075—2083, 2006.

[6] K. Otsuka and C.M. Wayman. *Shape memory materials*. Cambridge university press, 1999.

[7] D.J. Hartl, D.C. Lagoudas, F.T. Calkins, and J.H. Mabe. Use of a Ni60Ti shape memory alloy for active jet engine chevron application: I. thermomechanical characterization. *Smart Materials and Structures*, 19(1):015020, 2009.

[8] J. Diani, P. Gilormini, C. Frédy, and I. Rousseau. Predicting thermal shape memory of crosslinked polymer networks from linear viscoelasticity. *Int. J. Solids Struct.*, 49(5):793—-799, 2012.

[9] P. Butaud, D. Renault, B. Verdin, M. Ouisse, and G. Chevallier. In-core heat distribution control for adaptive damping and stiffness tuning of composite structures. *Smart Materials and Structures*, 29(6):065002, 2020.

[10] P. Butaud, V. Placet, J. Klesa, M. Ouisse, E. Foltête, and X. Gabrion. Investigations on the frequency and temperature effects on mechanical properties of a shape memory polymer (veriflex). *Mech. Mater.*, 87:50—-60, 2015.

[11] A. M. Schmidt. Electromagnetic activation of shape memory polymer networks containing magnetic nanoparticles. *Macromolecular Rapid Communications*, 27(14):1168–1172, 2006.

[12] Q. Ze, X. Kuang, S. Wu, J. Wong, S.M. Montgomery, R. Zhang, J.M. Kovitz, F. Yang, H.J. Qi, and R. Zhao. Magnetic shape memory polymers with integrated multifunctional shape manipulation. *Advanced Materials*, 32(4):1906657, 2020.

[13] B. Kiefer and D.C. Lagoudas. Magnetic field-induced martensitic variant reorientation in magnetic shape memory alloys. *Philosophical Magazine*, pages 4289—-4329, 2005.

[14] Y. Kim, H. Yuk, R. Zhao, S.A. Chester, and X. Zhao. Printing ferromagnetic domains for untethered fast-transforming soft materials. *Nature*, 558:274–291, 2018.

[15] S. Qi, H. Guo, J. Fu, Y. Xie, M. Zhu, and M. Yu. 3d printed shape-programmable magneto-active soft matter for biomimetic applications. *Composites Science and Technology*, 188:107973, 2020.

[16] E. Y. Kramarenko, A. V. Chertovich, G. V. Stepanov, A. S. Semisalova, L. A. Makarova, N. S. Perov, and A. R. Khokhlov. Magnetic and viscoelastic response of elastomers with hard magnetic filler. *Smart materials and structures*, 24(3):035022 (11p), 2015.

[17] L. Bodelot, J. P. Voropaieff, and T. Pössinger. Experimental investigation of the coupled magneto-mechanical response in magnetorheological elastomers. *Experimental Mechanics*, 58(2):207–221, 2018.

[18] S. Hermann, P. Butaud, G. Chevallier, J.-F. Manceau, and C. Espanet. Magnetic and dynamic mechanical properties of a highly coercive mre based on NdFeB particles and a stiff matrix. *Smart Mater. Struct*, 29:105009, 2020.

[19] M. Savary, S. Hermann, C. Espanet, V. Préault, G. Chevallier, P. Butaud, and J.-F. Manceau.

Development of a magneto-mechanical bench and experimental characterization of magneto-rheological elastomers. *IEEE Transactions on Magnetics*, 58(2):1–4, 2021.

[20] D.W. Pohl. Dynamic piezoelectric translation devices. *Review of scientific instruments*, 58(1):54–57, 1987.

[21] K. Spanner and B. Koc. Piezoelectric motors, an overview. In *Actuators*, volume 5, page 6. Multidisciplinary Digital Publishing Institute, 2016.

[22] D. Newton, E. Garcia, and G.C. Horner. A linear piezoelectric motor. *Smart Materials and Structures*, 7(3):295, 1998.

[23] T Takano, Y Tomikawa, T Ogasawara, S Sugawara, and M Konno. Ultrasonic motors using piezoelectric ceramic multimode vibrators. *IEEE transactions on ultrasonics, ferroelectrics, and frequency control*, 37(3):224–229, 1990.

[24] M. Amjadian and A.K. Agrawal. Planar arrangement of permanent magnets in design of a magneto-solid damper by finite element method. *Journal of Intelligent Material Systems and Structures*, 31(7):998–1014, 2020.

[25] S. Hermann, P. Butaud, R. de O. Teloli, J.-F. M., M. Savary, and G. Chevallier. Magnetically induced friction damping based on magnetoactive elastomers-a proof of concept. *Journal of Sound and Vibration*, page 117000, 2022.

[26] D. Hartl, B. Volk, D.C. Lagoudas, F. Calkins, and J. Mabe. Thermomechanical characterization and modeling of Ni60Ti40 sma for actuated chevrons. In *ASME international mechanical engineering congress and exposition*, volume 47659, pages 281–290, 2006.

[27] J. Ivens, M. Urbanus, and C. De Smet. Shape recovery in a thermoset shape memory polymer and its fabric-reinforced composites. *Express Polymer Letters*, 5(3):254—-261, 2011.

[28] C. Segui, E. Cesari, J. Pons, and V. Chernenko. Internal friction behavior of Ni-Mn-Ga. *Materials Science and Engineering: A*, 73(1–2):481–484, 2004.

Appendix A. Sets of pixel pairs used for the analysis of the local contact state on 13 positions at the interface

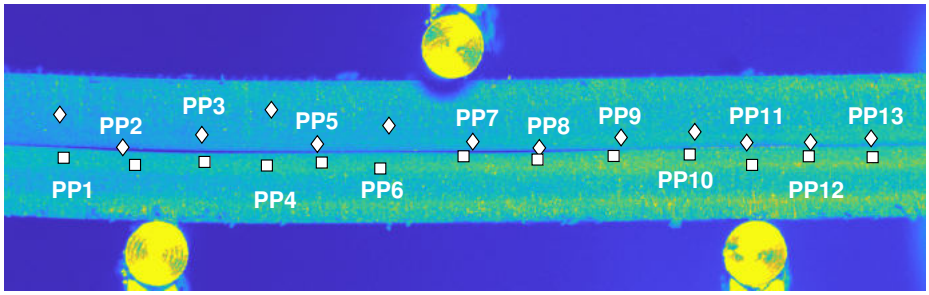

Figure A1. Choice of the pixel pairs (PP) along the MF-SMP for the test with $u_{cyc} = 1.5\,\text{mm}$. ◇ – pixel in upper beam, □ – pixel in lower beam

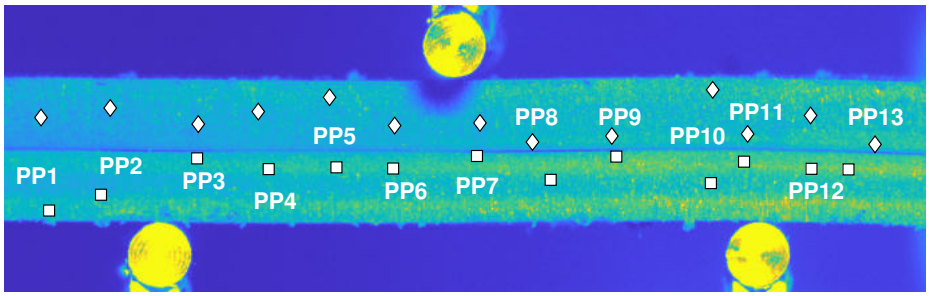

Figure A2. Choice of the pixel pairs (PP) along the MF-SMP for the test with $u_{cyc} = 3\,\text{mm}$. ◇ – pixel in upper beam, □ – pixel in lower beam

Appendix B. Glossary

Table B1. Glossary

Term	Definition
DIC	Digital Image Correlation
H-MAE	magnetically Hard MagnetoActive Elastomer
M-SMA	Magnetic Shape Memory Alloy
MAE	MagnetoActive Elastomer
MF	MagnetoFriction
PE	PiezoElectric
PP	Pixel Pair
SMA	Shape Memory Alloy
SMP	Shape Memory Polymer